Strain Localization and Weakening Processes in Viscously Deforming Rocks: Numerical Modeling Based on Laboratory Torsion Experiments

M. J. E. A. Döhmann[1,2*], S. Brune[1,2], L. Nardini[1], E. Rybacki[1], G. Dresen[1,2]

[1]GFZ German Research Centre for Geosciences, Telegrafenberg, 14473 Potsdam, Germany

[2]Institute of Earth and Environmental Sciences, University of Potsdam, Germany

* Corresponding author: Maximilian Döhmann (doehmann@gfz-potsdam.de)

Key points

- Simple numerical softening laws successfully reproduce strain localization and stress transients observed in laboratory torsion tests.
- A viscous process zone evolves at the tip of a nucleating shear zone and propagates with progressive shear strain.
- Strain weakening is required to form a localized shear zone in a strong matrix surrounding a weak inclusion.

Abstract

Localization processes in the viscous lower crust lead to the formation of deformation zones over a broad range of scales that may affect the mechanical response of faults in the upper crust during the entire seismic cycle. In order to gain detailed insight into the processes involved in strain localization and rheological weakening in viscously deforming rocks we conduct centimeter-scale numerical models. Our 2D Cartesian models are benchmarked to high-temperature and high-pressure torsion experiments on Carrara marble samples containing a single weak Solnhofen limestone inclusion. The numerical models successfully reproduce bulk stress-strain transients and final strain distributions observed in the experiments by applying a simple softening law that mimics rheological weakening. By varying softening parameter values within this modeling framework, we quantify the impact of rheological weakening on localization and shear zone formation.

We find that local stress concentrations forming at the inclusion tips initiate strain localization inside the host matrix. Rheological weakening is a precondition for shear zone formation within the matrix. At the tip of the propagating shear zone, weakening occurs within a process zone which expands with time from the inclusion tips towards the matrix. Shear zone width is found to be controlled by the degree of softening. Introducing a second softening step at elevated strain, a high strain layer develops inside the localized shear zone, analogue to the formation of ultramylonite bands in mylonites.

1. Introduction

Deformation localization is ubiquitous in earth materials and observed over a broad range of scales in space and time. Localization processes lead to the generation of deformation zones that separate less strained or unstrained parts of the lithosphere (Fossen & Cavalcante, 2017). In the brittle upper crust deformation is present as fault zones (Coyan et al., 2013; Valoroso et al., 2013) transitioning into localized ductile shear zones in the middle–lower crust at the brittle-ductile transition hosting mylonites and ultra-mylonites (Palin et al., 2014; Park & Jung, 2017). Localization within the deeper ductile lithosphere is accommodated by a combination of different deformation mechanisms (Kenkmann & Dresen, 2002; Burlini & Bruhn, 2005). These processes cause shear zone initiation at material heterogeneities and multiple defects commonly present in rocks that serve as nucleation points for shear zones on the micro- or macro-scale. Typical examples include randomly scattered flaws (e.g. Misra & Mandal, 2007), brittle fractures (Mancktelow & Pennacchioni, 2005), weak layers (Gerbi et al., 2015), veins or dykes (Handy, 1989) or rock fabric (Bürgmann & Dresen, 2008). A plethora of studies showed that a subsequent strength reduction in shear zones may be attributed to a range of different processes, like grain-size reduction (Tasaka et al., 2017), a change in controlling deformation mechanism such as from dislocation to diffusion creep (e.g. White, 1976; Handy, 1989; Linckens et al., 2011), shear heating (Duretz et al., 2015), the development of crystallographic preferred orientations (Ji et al., 2004) or melting (Handy et al., 2001).

Laboratory experiments on rock materials provide insights into localization and weakening processes during shear zone formation at well-defined deformation conditions. A number of experimental studies have investigated strength and microstructures in high-strain deformation tests on monomineralic geomaterials (Bystricky et al., 2000; Pieri et al., 2001a; Pieri et al., 2001b; Ter Heege et al., 2001; Barnhoorn et al., 2004; Hansen et al., 2012) and multiphase aggregates (Bruhn & Casey, 1997; Bruhn et al., 1999; Rybacki et al., 2003; Dimanov & Dresen, 2005; Bystricky et al., 2006). The effect of material heterogeneities on the rheological response of otherwise homogeneous earth materials has been recently addressed by Rybacki et al. (2014), who analyzed the effect of material heterogeneities on the onset of localized viscous deformation.

In addition to experimental studies, numerical modeling of localization processes allows testing realistic materials in order to isolate the effect of specific deformation mechanisms and parameters. Previous numerical modeling work aimed at understanding the role of strength anisotropies that are either caused by compositional differences (Kenkmann & Dresen, 1998; Mancktelow, 2002; Treagus & Lan, 2004; Cook et al., 2014) or due to inherited structures (Corti et al., 2007; Mazzotti & Gueydan, 2017; Webber et al., 2018). For example, during lithospheric extension the inherited mechanical structure exerts a strong control on rift geometry and architecture (Duretz et al., 2016). Material heterogeneities significantly impact strain localization: (1) Hard inclusions produce stress concentrations inside a homogeneous matrix, and (2) weak inclusions localize strain in turn producing stress concentrations at the inclusion matrix interface (Cyprych et al., 2016). Jammes et al. (2015) identified three end-member types of shear zones: (1) localized, (2) localized anastomosing and (3) delocalized shear zone that depend on the proportion of strong and weak phase and the strength ratio. Other modeling studies focused on the effect of rheological weakening and hardening mechanisms. Numerical weakening mechanisms may depend on strain (Cyprych et al., 2016; Mazzotti & Gueydan, 2017), stress (Gardner et al., 2017), or deformation work or use grain size evolution in combination with grain-size dependent flow laws (e.g. Jessell et al., 2005; Herwegh et al., 2014; Cross et al., 2015) and all of them have been shown to strongly influence the localization behavior in numerical models. Some form of weakening is required to localize strain in an otherwise homogeneous rock matrix as observed in nature (Ellis et al., 2001), experiments (Rutter, 1999), and models (Gueydan et al., 2014).

Here we compare the results of our numerical models to a series of laboratory tests (Nardini et al., 2018) in order to investigate the temporal and spatial evolution of strain localization and weakening processes in viscously deforming rocks. For simplicity, we use a single weak inclusion torsion setup and analyze dynamics, strength, and geometry of the resulting ductile shear zone. With additional numerical tests we extend the scope of this study to the impact of weakening on localization behavior and shear zone formation.

2. Numerical modeling of torsion experiments

2.1. Setup of the laboratory experiments

Sample preparation is following the procedures described in Rybacki et al. (2014): Cylinders of Carrara marble (10 mm in length, 15 mm outer diameter) were cut from a single block of marble, and an internal borehole (6.1 mm of inner diameter) was cored and subsequently filled with cylinders of solid gold to provide a homogeneous distribution of stress over the entire sample through the full duration of the experiments (Paterson & Olgaard, 2000). Circular segments of Solnhofen limestone (arc length ~11.8 mm), a very fine grained (average grain size < 10 µm) rock, were produced by polishing ~750 µm thick sections that were subsequently inserted in the external surface of the Carrara marble cylinders (see Figure 1a).

Experiments were conducted in a Paterson-type gas deformation apparatus (Paterson, 1970), at 900 °C temperature and 400 MPa confining pressure. The samples were inserted in copper jackets of ~0.2 mm thickness, and jacket strength at the experimental conditions was accounted for in the evaluation of the mechanical data. Straight vertical scratches on the jacket surface serve as passive strain markers. As shown in Rybacki et al. (2014), at experimental P-T conditions the fine grained limestone is substantially softer than Carrara Marble and therefore acts as a weak material heterogeneity within a homogeneous stronger matrix. Two different loading conditions, constant twist rate (equivalent to a strain rate of $1.9*10^{-4}$ s^{-1} at the outer periphery) and constant torque (~18.8 MPa), were tested. For each loading type, samples were tested to a final bulk shear strain γ ~1 (Nardini et al., 2018).

2.2. Numerical modeling technique

In this study, we use the geodynamic modeling software SLIM3D (Semi-Langrangian Implicit Model for 3 Dimensions) (Popov & Sobolev, 2008). The implicit finite element code utilizes the Arbitrary Lagrangian-Eulerian Method, has a realistic elasto-visco-plastic formulation for rheology and a free surface. The software was originally designed to investigate lithospheric-scale processes and has since been applied in divergent (Brune et al., 2012, 2013, 2016, 2017; Brune & Autin, 2013; Brune, 2014; Heine & Brune, 2014; Koopmann et al., 2014; Clift et al., 2015), convergent (Quinteros et al., 2010; Quinteros & Sobolev, 2013; Duesterhoeft et al., 2014) and transform (Popov et al., 2012; Brune, 2014) plate boundary settings. Recently however, its scope has been extended with the aim to investigate localization processes on the centimeter-scale (Cyprych et al., 2016).

With the SLIM3D software, we solve the thermomechanically coupled conservation equations of momentum

$$-\frac{\partial p}{\partial x_i}+\frac{\partial \tau_{ij}}{\partial x_j}+\rho g_z=0 \tag{1}$$

energy

$$\rho C_p \frac{DT}{Dt}-\frac{\partial}{\partial x_i}\left(\lambda \frac{\partial T}{\partial x_i}\right)-\tau_{ij}\dot{\varepsilon}_{ij}=0 \tag{2}$$

and mass

$$\frac{1}{K}\frac{Dp}{Dt}-\alpha_T\frac{DT}{Dt}+\frac{\partial v_i}{\partial x_i}=0 \tag{3}$$

with coordinates x_i, velocities v_i, temperature T, time t, pressure p, stress deviator τ_{ij}, strain rate deviator $\dot{\varepsilon}_{ij}$, densities ρ, gravity vector g_z, heat capacities C_p, heat conductivities λ, thermal expansivities α_T, and bulk moduli K. The Einstein summation convention is applied over repeated indices.

The conservation equations are solved simultaneously considering the constitutive laws that relate deformation and stress. Total deviatoric strain rate is described as the sum of elastic and viscous strain rate (Simo & Hughes, 2006):

$$\dot{\varepsilon}_{ij} = \dot{\varepsilon}_{ij}^{elastic} + \dot{\varepsilon}_{ij}^{viscous} = \frac{1}{2G}\hat{\tau}_{ij} + \frac{1}{2\eta_{eff}}\tau_{ij} \tag{4}$$

where G is the elastic shear modulus, $\hat{\tau}_{ij}$ the objective stress rate (e.g. Bonet & Wood, 1997), and η_{eff} the effective viscosity.

We use dislocation creep flow laws to model the viscous deformation of limestone and marble. The effective viscosity is described as:

$$\eta_{eff} = \frac{1}{2}\tau_{II}\dot{\varepsilon}_{dis}^{-1} \tag{5}$$

with τ_{II} as the second invariant of the effective deviatoric stress given by:

$$\tau_{II} = \sqrt{\frac{1}{2}(\sigma_{xx}-p)^2 + \frac{1}{2}(\sigma_{yy}-p)^2 + \frac{1}{2}(\sigma_{zz}-p)^2 + \sigma_{xy}^2 + \sigma_{xz}^2 + \sigma_{yz}^2} \tag{6}$$

and $\dot{\varepsilon}_{dis}$ as the second invariant of the viscous strain rate for dislocation creep, which is defined as:

$$\dot{\varepsilon}_{dis} = B_{dis}(\tau_{II})^n \exp\left(-\frac{E_{dis}}{RT}\right) \tag{7}$$

where B_{dis} is the material-dependent creep parameter or pre-exponential factor, n the power law stress exponent, E_{dis} the activation enthalpy and R the gas constant (Popov and Sobolev, 2008). Flow law parameters for Carrara marble and Solnhofen limestone are given in Table 1.

To account for the rheological weakening mechanisms operating in rocks at elevated temperatures and pressures, we implement a function that captures progressive weakening for each element by increasing the pre-exponential factor (B_{dis}) linearly between two accumulated finite viscous strain threshold values (ε_1 and ε_2) by a fraction of factor A depending on the actual viscous strain ε of the element:

$$B_{dis} = B_{dis0} * \begin{cases} 1 \ if \ \varepsilon < \varepsilon_1 \\ 1 + \frac{A-1}{\varepsilon_2 - \varepsilon_1}(\varepsilon - \varepsilon_1) \ if \ \varepsilon_1 < \varepsilon < \varepsilon_2 \\ A \ if \ \varepsilon < \varepsilon_2 \end{cases} \tag{8}$$

The threshold values ε_1 and ε_2 depend either on 1) accumulated viscous strain (see Cyprych et al., 2016) or 2) deformation work per element volume W_{def} defined as:

$$W_{\mathrm{def}} = \varepsilon_{visc} * \tau_{II} \tag{9}$$

with ε_{visc} as the viscous component of finite strain, which is computed by integrating the second invariant of the deviatoric viscous strain rate tensor with respect to time. As a result, this parameterization reduces the effective viscosity by an arbitrary factor A, which we call the weakening amplitude (see Figure 1b). The thresholds ε_1 and ε_2 of the baseline model are motivated by experimental observations. For example, in torsion experiments on solid Carrara marble, Pieri et al. (2001b) found that samples are fully recrystallized at bulk strains > 2.

2.3. Setup of the numerical model

Our 2D Cartesian models are designed to reproduce the single inclusion experiments of Nardini et al. (2018) described above. We model the laboratory shear deformation of a hollow cylinder by using periodic boundary conditions, such that material leaving one side of the model in shear direction enters again on the opposite side (see Figure 1c). The model height is 10 mm and the length of the model along shear direction is 47.124 mm which represents the outer circumference of the hollow cylinder in the laboratory experiment. Thermal properties of the material do not influence the model results, due to an imposed temperature of 900 °C and the small model size. To compare with the experiments, we apply constant strain rate and constant stress boundary conditions, respectively.

Flow laws implemented in the models are based on a series of torsion and triaxial experiments performed on Carrara marble and Solnhofen limestone by Rybacki et al. (2014). The flow laws are similar to those obtained by Schmid et al. (1980). Activation energy and thus temperature dependency are incorporated into a material-dependent creep parameter (B_{dis0}), as the experiments and models are performed at a constant temperature (900 °C) (see Table 1).

Table 1: Flow laws and boundary conditions for the reference model. Temperature dependence is incorporated in the pre-exponential factor and flow law parameters are valid for given boundary conditions only (Rybacki et al. 2014).

	Flow laws		Boundary conditions	
Phase	n	log(B_{dis0}) [Pa^{-n} s^{-1}]	T [°C]	*strain rate* [s^{-1}]
Carrara marble (matrix)	7.6[a,b]	-59.59[a]	900	$1.9*10^{-4}$
Solnhofen limestone (inclusion)	1.4[a]	-13.10[c]		

[a]Rybacki et al. (2014)

[b]Schmid et al. (1980)

[c]Rybacki et al. (2014) report -12.55; was modified such that peak stress of model is equivalent to experiment

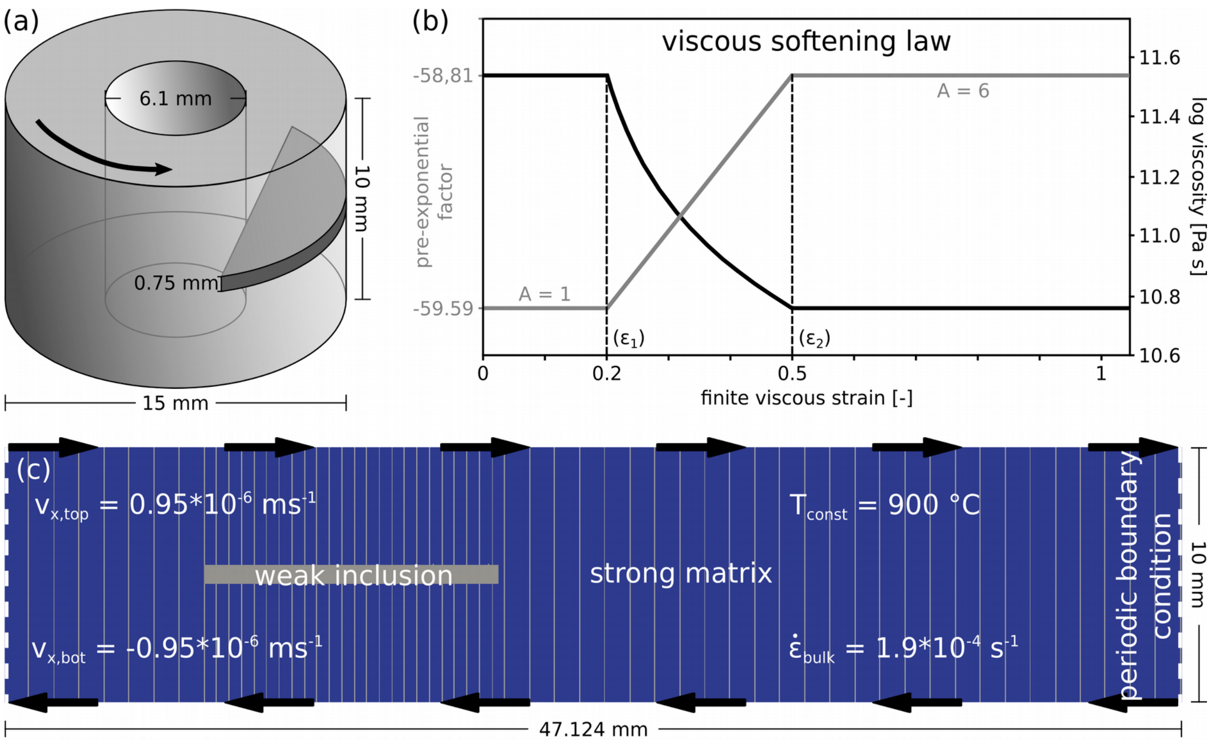

Figure 1: (a) Schematic drawing of experimental setup: cylinder height is 10 mm, outer diameter is 15 mm, the inclusion has an angular length of 90° and the inner borehole has a diameter of 6.1 mm and is filled with a solid gold cylinder. The matrix consists of Carrara Marble and the inclusion of Solnhofen limestone. (b) Effect of viscous softening on Carrara marble flow law. The pre-exponential factor A (weakening amplitude) is increased between the two threshold values of local finite strain ε_1 and ε_2, hence the effective viscosity is locally reduced. (c) Model setup and boundary conditions. Constant bulk strain rate ($\dot{\varepsilon}_{bulk}$) is achieved by prescribing velocity at top ($v_{x,top}$) and bottom ($v_{x,bot}$) model boundaries. At the left and right model side we use periodic boundary conditions, i.e. velocity and stress are continuous across these boundaries and any material point crossing these boundaries enters again on the other side of the model. Flow laws of matrix and inclusion are chosen to represent Carrara marble (strong matrix) and Solnhofen limestone (weak inclusion) (see Table 1). Vertical gray lines are passive strain markers.

3. Numerical modeling of single weak inclusion torsion experiments

In the following, we examine (1) the mechanical results, (2) the results of our numerical model in comparison to benchmark tests, (3) the evolution of the model, (4) the role of softening, (5) the effect of varying softening parameters, and (6) the impact of progressive softening. Points (2) and (3) combined with (1) yield further insights into the strain localization process. With (4) to (6) we expand the parameter space beyond the experimental results allowing new insights from the numerical perspective.

3.1. Torsion experiment results

At constant twist rate, calculated shear stress at the sample periphery initially increased up to a peak value of ~19–20 MPa up to a bulk shear strain of γ ~0.2, followed by gradual weakening up to the maximum bulk shear strain of about 1 for sample CMHT-17 (Figure 2a). This sample is used to benchmark the numerical model. In the constant torque experiment, torque was kept constant such that the maximum shear stress at the sample periphery was about 18.8 MPa, similar to the peak stress measured in the constant twist rate experiment (see supplementary Figure S1 for results of the constant torque experiment and a comparison to a numerical model).

3.2. Benchmarking of the numerical model

The benchmark comparison reveals two differences between model and experiments. First, when using the experimentally determined flow laws, we find that the maximum bulk shear stress of the model is ~5 % lower than in the experiment. Likely, this offset is due to experimental uncertainties contained in the flow laws, which we level out by adopting a slightly smaller pre-exponential factor for the Solnhofen inclusion (Table 1). The second and most important difference between model and experiment results from simulating pure dislocation creep of the matrix. This ignores any other mechanism that might contribute to deformation such as twinning and grain boundary sliding. However, the experimental results are successfully reproduced using a model based on the implemented strain-dependent softening mechanism with following values for the accumulated finite strain thresholds: ε_1 = 0.2, ε_2 = 0.5 and the weakening amplitude: A = 6 (Figure 1b) affecting the Carrara marble.

Our model results are in excellent agreement with experimental results at constant strain rate (CMHT-17). Stress strain curve (see Figure 2a), shear zone width and matrix deformation are very similar as shown by the passive strain markers (see Figure 2b,c). The inclusion length fits to the experimental estimate and its distorted rhomboidal shape (Rybacki et al., 2014) is also observed in the model. Steady-state deformation is not yet reached at a bulk shear strain of $\gamma = 1$, indicated by the negative slope of the stress strain curve. Constant stress model and experimental results are in good agreement as shown in the supplements (Figure S1). The test also indicates that both loading configurations (constant strain rate and constant stress) lead to nucleation of ductile shear zones.

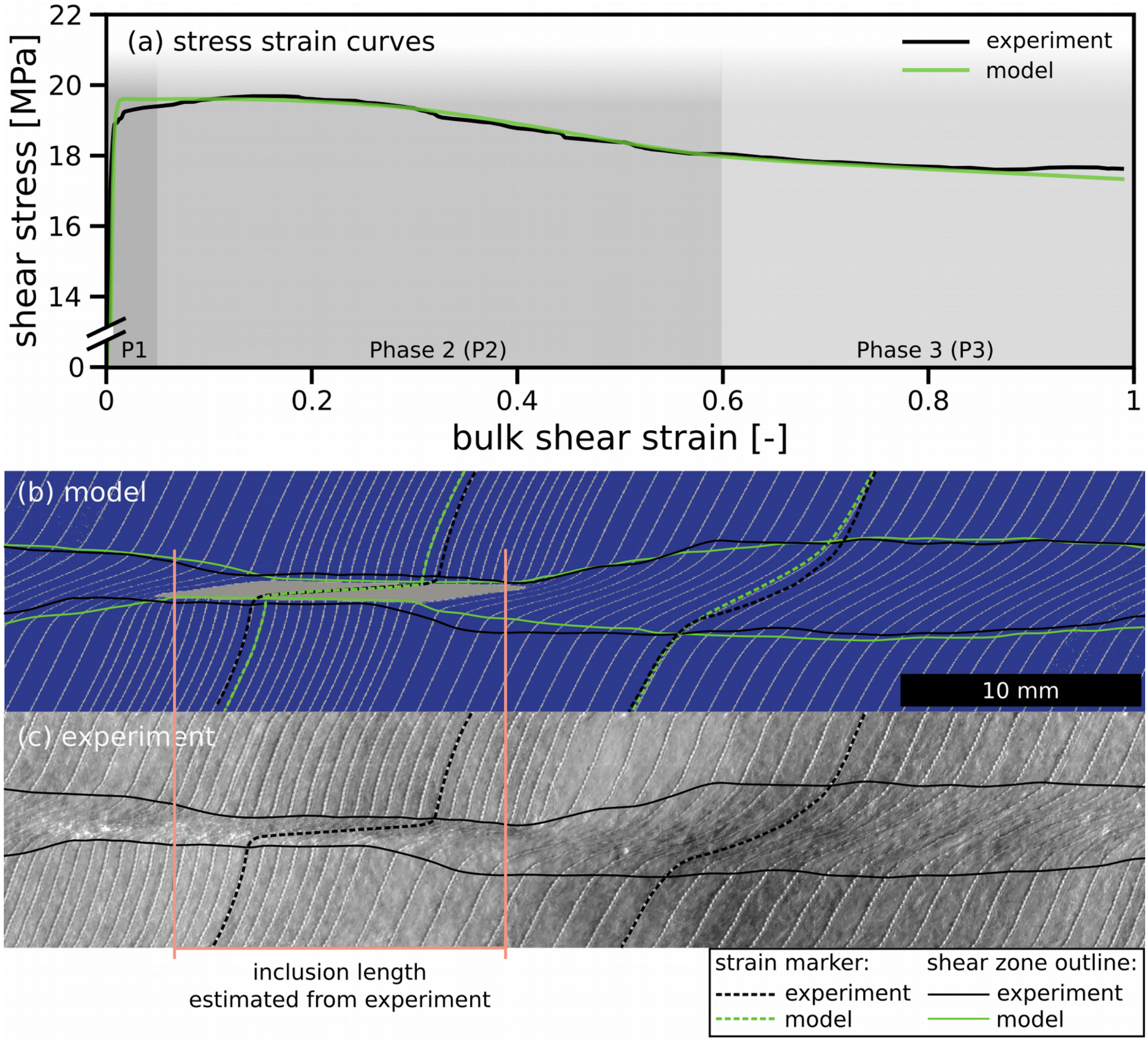

Figure 2: Benchmark and comparison of constant strain rate model to experiment. (a) Stress strain curves of reference model (green) and experiment (black). Background shows the phases P1 – pre-weakening, P2 – onset and acceleration of weakening and P3 – deceleration of weakening. (b) Model with passive strain markers and shear zone outlines of model (green) and experiment (black). (c) Copper jacket from experiment with passive strain markers, estimated inclusion length and shear zone outline. Results in (b) and (c) are shown at a bulk shear strain of ~1.

3.3. Spatial and temporal model evolution

In this section we analyze the bulk stress evolution by analyzing the evolution of model-intrinsic strength variations. To describe inhomogeneous deformation surrounding the shear zone tip we use the term *process zone* analogue to nonlinear fracture mechanics (Zang et al., 2000). Here we expand its meaning to viscous materials describing a region of enhanced microstructural modification in comparison to the remaining matrix (Rybacki et al., 2014). To analyze the evolution of the process zone that is observed in the experiments, we visualize the stress and strain distribution in space and time. Four phases (P1–P4) may be distinguished during the model evolution: *pre-weakening* (P1), *onset and acceleration of weakening* (P2), *deceleration of weakening* (P3) and *steady-state* (P4). In phase P1 stresses build up (loading) and no material is weakened by viscous softening, but with ongoing deformation the shear strain locally exceeds the threshold strain ε_1 defining the beginning of weakening and phase P2 at a bulk shear strain of γ ~0.05. With progressive deformation the process zone enlarges and a larger volume exceeds the weakening threshold, accelerating bulk softening. At a bulk shear strain of γ ~0.6 the process is slowing down defining the beginning of P3. Two fully weakened regions in the model center emerge and locally shear strain exceeds ε_2 that defines the second threshold and completion of weakening. In phase P4 the deformation proceeds at steady state, which is only observed for bulk shear strains γ > 2 using the benchmark setup. In the benchmark model steady state is not reached since the test is terminated at a bulk shear strain of γ ~1.

Pronounced stress peaks in front of the inclusion tips are observed during early stages of deformation (P1 and early P2) (see Figure 3a) resulting in higher strain rates (Figure 3g) than in surrounding matrix regions of low stress. Similar to the experimental results, strain rates in the process zone are locally increased by up to a factor of ~50 in comparison to the matrix. Due to this stress and thus strain rate differences, the finite strain threshold value ε_1 (white outline) is first exceeded at the inclusion tips where softening of the material starts. Strain rate subsequently increases further and soon the second threshold value ε_2 (black outline) is also exceeded indicating local completion of softening (see Figure 3b–f&h–l). Consequently, stress gradually decreases again locally between the onset outline and the inclusion (see Figure 3b&c). The stress concentrations at the inclusion tips remain due to the remaining viscosity contrast between matrix and inclusion. The cylindrical symmetry of the experiment and our model results in a merge of the two weakening fronts (ε_1 outline). Once the two local stress peaks causing the onset of softening merge, they combine to a single, local stress maximum in the model center and the stress gradient in the process zone decreases significantly with further deformation (see Figure 3e). The fully weakened zones grow, as the process zone propagates into the matrix from the inclusion, featuring a gradual stress increase from the end of softening outline towards the inclusion tips (see Figure 3d). In phase P3 the completely weakened areas in the vertical model center are connected (see Figure 3e&k), after which the rate of weakening decreases (Figure 2a). Stress and strain rates directly above and below the inclusion remain low throughout the experiment due to local stress partitioning. A small transition zone between the inclusion and matrix exists due to coupling of the materials. The overall observed stress drop in the matrix (Figure 3a-f) is due to the increase of the pre-exponential factor by the softening law, which in return decreases the effective viscosity by a preset factor A.

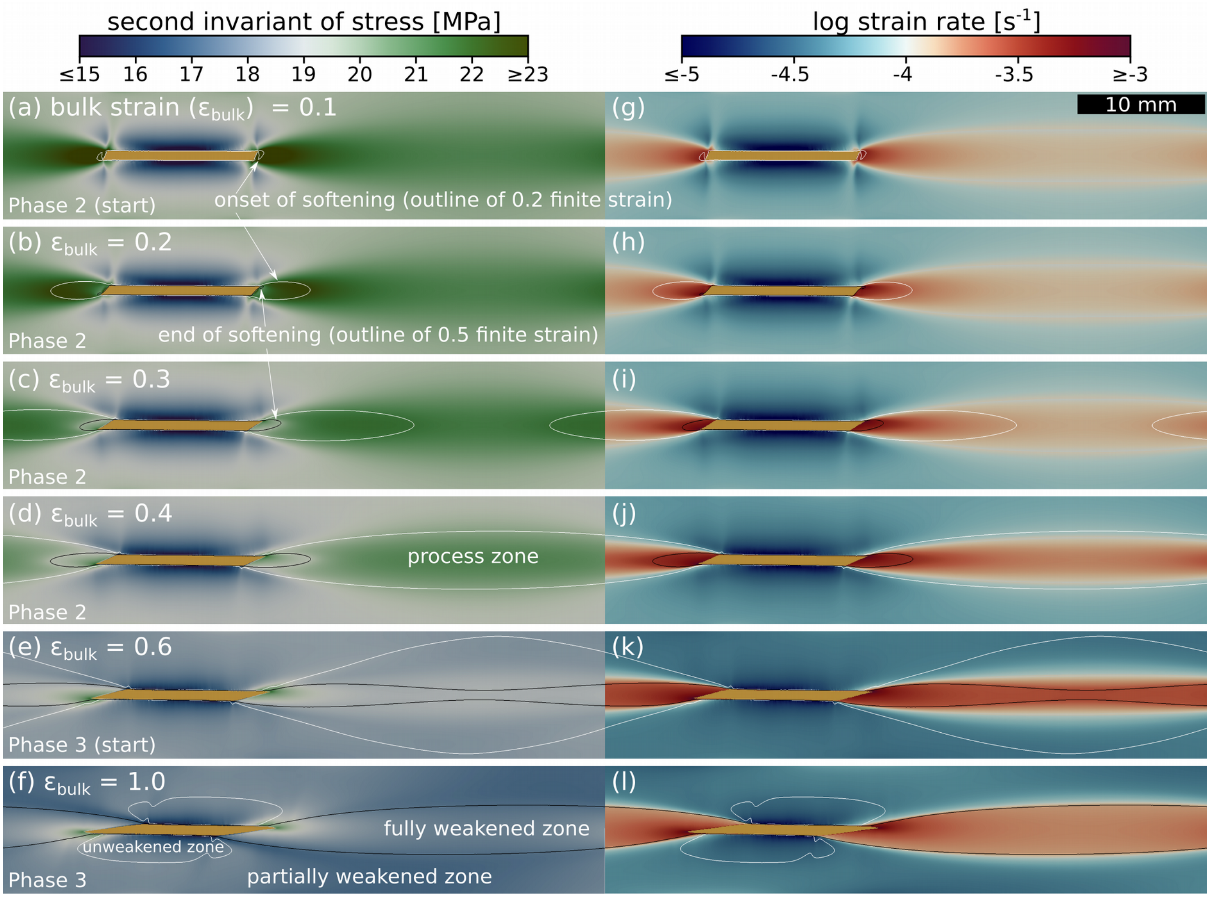

Figure 3: Local Stress (a-f) and strain rate (g-l) evolution within the matrix of the constant strain rate benchmark model. Outlines indicate finite strain thresholds of ε_1 = 0.2 for beginning (white) and ε_2 = 0.5 for end (black) of softening. The process zone is associated with a local stress maximum propagating into the matrix (a-c). The zone is controlled by the onset and end of softening. A second stress peak remains fixed at the inclusion tips (a-f).

Analytical solutions of linear dislocation in an elastic half-space predict elevated stresses as displacements vanish towards fracture tips (Okada, 1985). Within the ductile regime and for inclusions of finite width, however, we find that the localization process at the inclusion tip evolves in a more complex way. Figure 4 shows length profiles that display key parameter values and their evolution with increasing bulk strain along two horizontal model cross sections. The position of profile (a) is chosen such that it crosses the center of the right inclusion tip at a bulk shear strain of 1 which is 0.1 mm above profile (b) along the model center. Horizontal velocity in profile (a) is increased, due to the vertical shift in position. By that, the point symmetry to the inclusion center is broken, which on the other hand is a feature of profile (b). Similar to a dislocation in an elastic medium, the area surrounding the inclusion tip exhibits high gradients in deformation and stress. The profiles show the highest strain rates and strains inside the weak inclusion directly at the tip. Highest stress values are however observed in the matrix in front of the inclusion. Local strain in the process zone at the inclusion tip increases approximately linear with bulk strain by a factor of four.

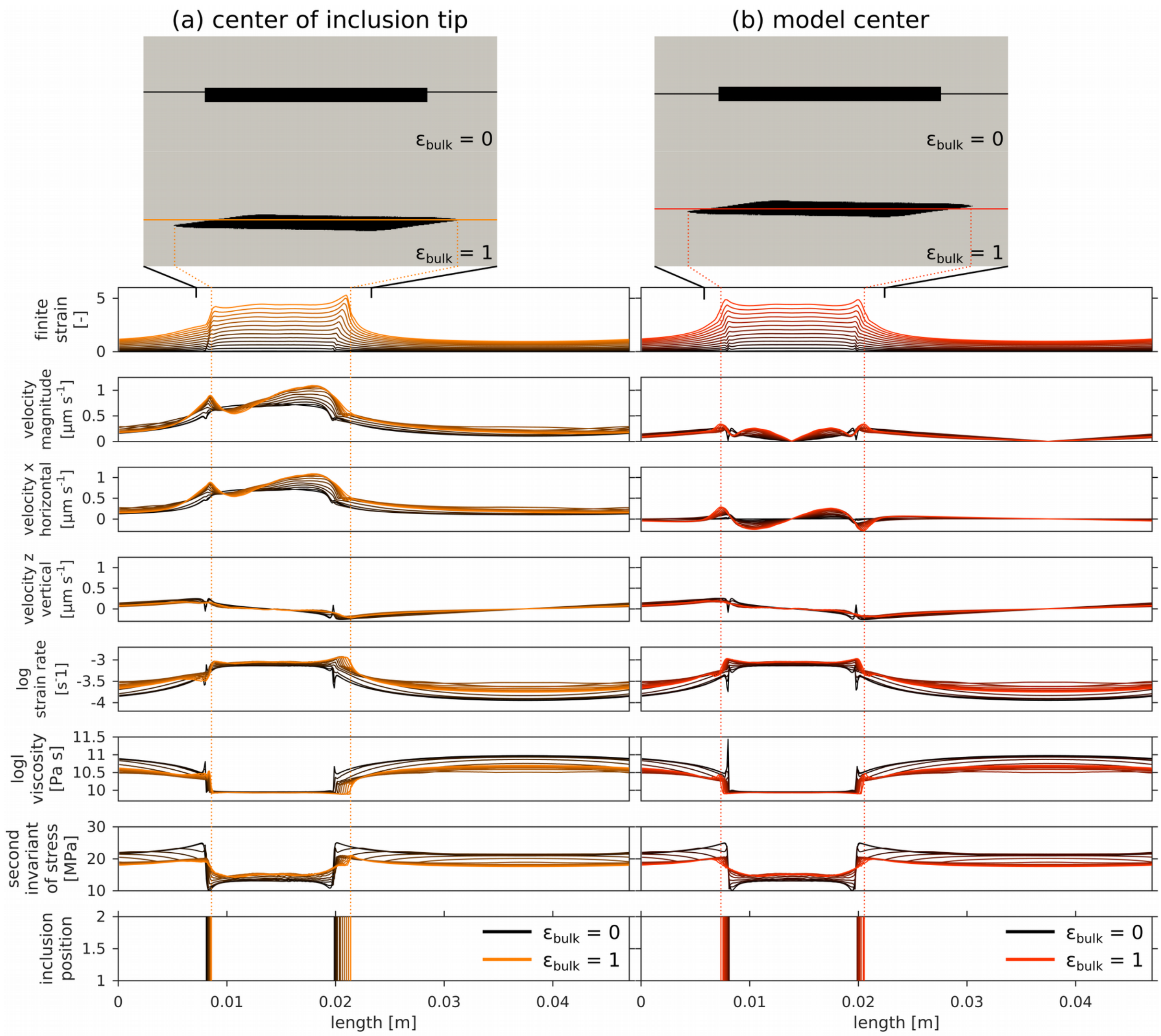

Figure 4: Along-strike variations of key parameters. The inclusion deforms due to simple shear generating differences between horizontal profiles at various vertical positions. Here we show profiles along the center of the inclusion (at a bulk strain of 1) and along the center of overall model domain. (a) Profile along the center of the inclusion tip. Maximum rate of deformation and accumulated finite strain are found in the inclusion tip and maximum stress in the matrix directly in front of the inclusion tip. (b) Profile along the model center. Due to the symmetry of the setup, results are approximately point symmetric to the model center.

3.4. The effect of softening on the benchmark model results

To better constrain the effect of the viscous softening formalism, we run an additional constant strain rate model, without the strain dependent formalism. Besides the differences in the stress strain curves (Figure 5a), there is also a less pronounced shear zone development (Figure 5b). This is indicated by the linearly deflected, green strain marker crossing the matrix and the green shear zone outline. Strain is instead localizing mainly in the inclusion and, to a lesser extent, in the matrix close to the inclusion tips. Nonetheless, the results of this test still show reasonable agreement with the experimental data, because the bulk weakening is generally low for the used samples and setup, which is indicated by the total shear stress drop of just ~2 MPa in the experiment. Additionally, we test a softening law that is based on deformation work instead of finite strain as discussed above. In this formulation, the weakening thresholds (ε_1 and ε_2, Eq. 8) are not based on finite strain, but on deformation work as defined in Eq. 9. However, we find no relevant difference to the strain based softening implementation (see supplementary Figure S2).

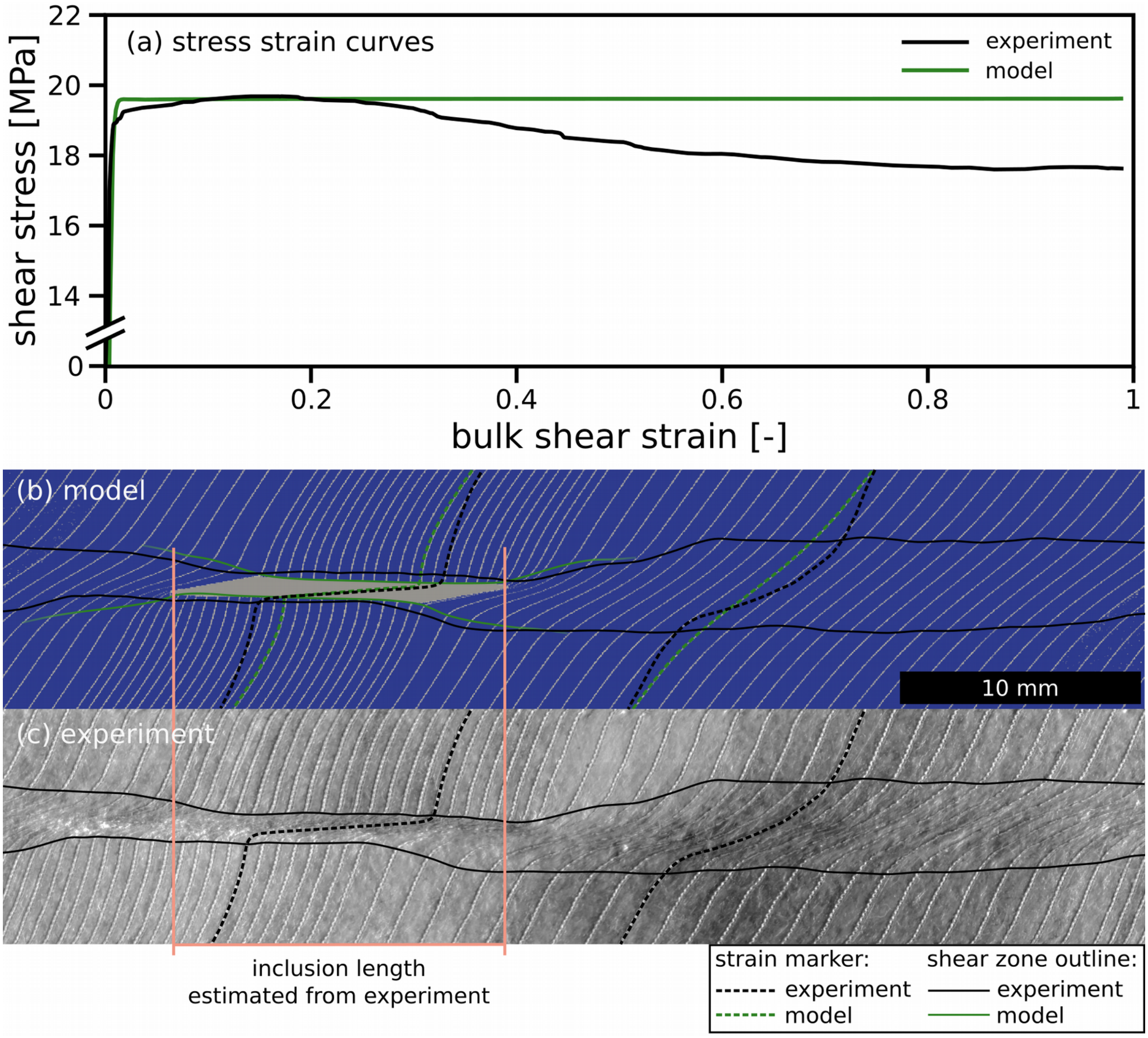

Figure 5: Comparison of model without softening to experiment (same as in Figure 2c). (a) Stress strain curves of model (green) and experiment (black). (b) Model with passive strain markers and shear zone outlines of model (green) and experiment (black). (c) Copper jacket from experiment with passive strain markers, estimated inclusion length and shear zone outline. Results in (b) and (c) are shown at a shear strain of ~1. In comparison to the reference model, shear stress remains constant over time and the shear zone in the matrix is less pronounced.

3.5. The softening law parameters

This chapter depicts the effects of the softening law parameters on the localization process. We therefore vary the three controlling parameters (Figure 1b): Two finite strain threshold values *onset* (ε_1) and *end* (ε_2), as well as the *weakening amplitude* (A). In order to test the effect of varying A, we change this parameter between 1 and 500 leavening the remaining benchmark model unchanged i.e. ε_1 (0.2) and ε_2 (0.5) (Table 2). Models are run up to a bulk shear strain of 4, where steady state conditions are reached in most cases. The reference model for instance reaches steady state at a bulk shear strain of approximately 2 (Figure 6a). Increasing A amplifies the weakening of the Carrara marble matrix, resulting in a bulk shear stress drop and enhanced strain and thus shear zone localization, which is also indicated by a decreasing angle between inclusion and matrix shear zone (Figure 6). Large values of A also increase the rate of strain localization. This is indicated by the sudden shear stress drop at about a bulk shear strain of 0.4 and by faster stress peak propagation into the matrix. For values A > 50 the matrix separates into two zones of substantial viscosity contrast (Figure 6b).

In another experiment, models are run up to a bulk shear strain of 4, varying ε_1 and ε_2 at constant A (Table 3). As expected this shifted the onset and end of weakening – earlier for lower finite shear strain values and later for higher – but the actual effect on the model is not linear (Figure 7a). Note that by changing the strain range of softening $\Delta\varepsilon = \varepsilon_1 - \varepsilon_2$, the slope of the stress strain curve and thus localization rate is affected as well. The reference model with the lowest $\Delta\varepsilon$ displays the fastest localization rate, because the rate with which the pre-exponential factor is increased is higher between the two thresholds due to the linear nature of the softening law. Model E2 with $\Delta\varepsilon$ of 0.8 however, reaches steady state only after a long period of ongoing softening (between 0.4 and 3.4 bulk shear strain). The local stress pattern of the tested models differ at a bulk shear strain of 1, depending on the applied threshold values. While model M0 is in the pre-weakening phase P1, model E3 & E2 are in phase P2 and model M1 & E1 already reached phase P3 approaching steady-state conditions (Figure 7b).

Table 2: Parameters for models used to test the effect of the weakening amplitude (A) of the softening law.

Models for testing weakening amplitude A	ε_1	ε_2	$\Delta\varepsilon$	A
M0 - no softening	-	-	-	1
M1 - reference model	0.2	0.5	0.3	6
A1	0.2	0.5	0.3	20
A2	0.2	0.5	0.3	100
A3	0.2	0.5	0.3	500

Table 3: Parameters for models used to test the effect of onset (ε_1) and end (ε_2) of the softening law.

Models for testing onset and end	ε_1	ε_2	$\Delta\varepsilon$	A
M0 - no softening	-	-	-	1
M1 - reference model	0.2	0.5	0.3	6
E1	0.0	0.5	0.5	6
E2	0.2	1.0	0.8	6
E3	0.5	1.0	0.5	6

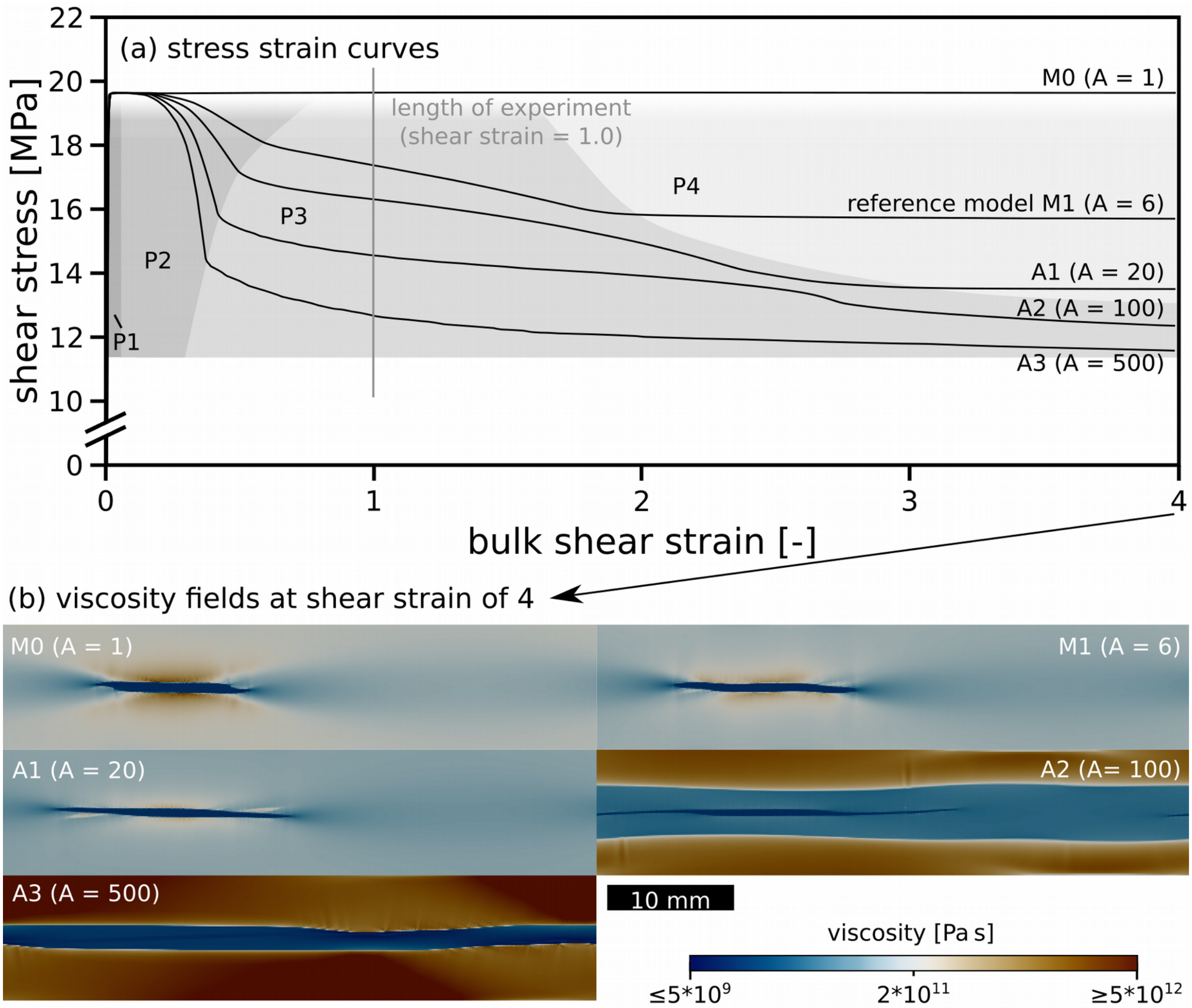

Figure 6: Effect of the weakening amplitude A. (a) Stress strain curves of models with different weakening amplitude. For comparison the length of the torsion experiment is indicated. P1–P4 refer to the phases described in chapter 3.3: *pre-weakening* (P1), *onset and acceleration of weakening* (P2), *deceleration of weakening* (P3) and *steady-state* (P4). (b) Viscosity fields of the models at a bulk shear strain of 4. The inclusion in the reference model is elongated further than in the model without weakening, as the matrix is increasingly deformed due to the softening law. This effect increases with A. For values of A > 50, strain localization is strongly pronounced, as shown by the viscosity field of models with a weakening amplitude A of 100 and 500. Higher values of weakening amplitude lead to stronger weakening and localization.

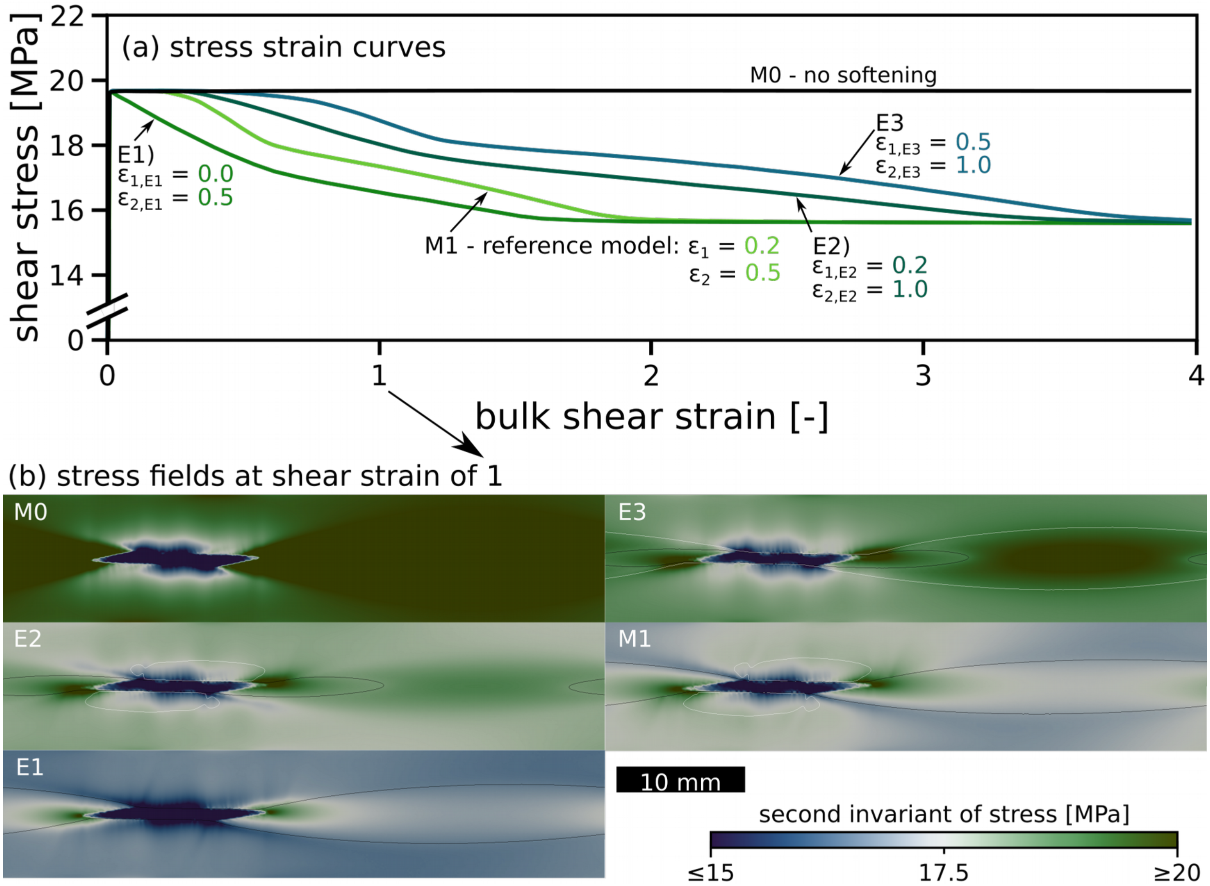

Figure 7: Effect of onset and end of weakening on the stress strain evolution. (a) Stress strain curves of models with varying onset (ε_1) and end parameters (ε_2). Note the shapes of curves E1 and E3 (same $\Delta\varepsilon$) indicating a non linear relationship between threshold parameters and weakening behavior. (b) Stress field of models at bulk shear strain of 1. M0) no softening; M1) reference model; E1) ε_1 = 0; E2) ε_2 = 1; E3) ε_1 = 0.5 and ε_2 = 1.0. Models with lower ε_1 have lower bulk strengths at the same bulk shear strain.

3.6. Ultramylonite model – the effect of progressive softening and deformation mechanism change

Mylonitic shear zones often feature mm–cm wide bands with fine grain sizes referred to as ultramylonites (Hippertt & Hongn, 1998; Kenkmann & Dresen, 2002). It is commonly assumed that grain size refinement from cataclasis, dynamic recrystallization or mineral reactions promotes a switch to grain size-sensitive deformation (Heitzmann, 1987; Bürgmann & Dresen, 2008). In order to mimic a progressive change in mechanism, a second softening step is introduced using a similar approach as described above for the onset of weakening (Eq. 8). Configuration of the model setup and the initial onset of softening are identical to the benchmark model, hence earliest stages of model evolution will be the same as before. The introduction of a second softening step with progressive strain, however, is expected to lead to further localization and formation of a narrow low-viscosity layer embedded in the primary shear zone. To this end finite strain thresholds for onset of weakening (ε_3 = 1) and completion (ε_4 = 2) are chosen, respectively. This procedure enables formation of a localized 'ultramylonite' band inside the active shear zone. A high weakening amplitude (A_u = 20) is chosen to enable fast and strong localization once the threshold ε_3 is reached.

Evolution of the model is equivalent to the benchmark model up to a bulk strain of ~0.4 (compare Figure 3a-d to Figure 8a-d). Upon onset of the second softening stage, strain localizes into a narrow zone in the model center (Figure 8n,o). Inside this high strain zone, the inclusion is strongly elongated and an anastomosing shape of the second shear zone establishes (Figure 8q,r) that additionally becomes wider with increasing bulk strain (Figure 8o-r). This transition to an anastomosing shape takes place due to a rotation, which is caused by the shear deformation that the material is subjected to. These results show that a second weakening stage due to a switch in mechanism may explain classical observations from mylonites, such as within the Castione marble zone (Heitzmann, 1987).

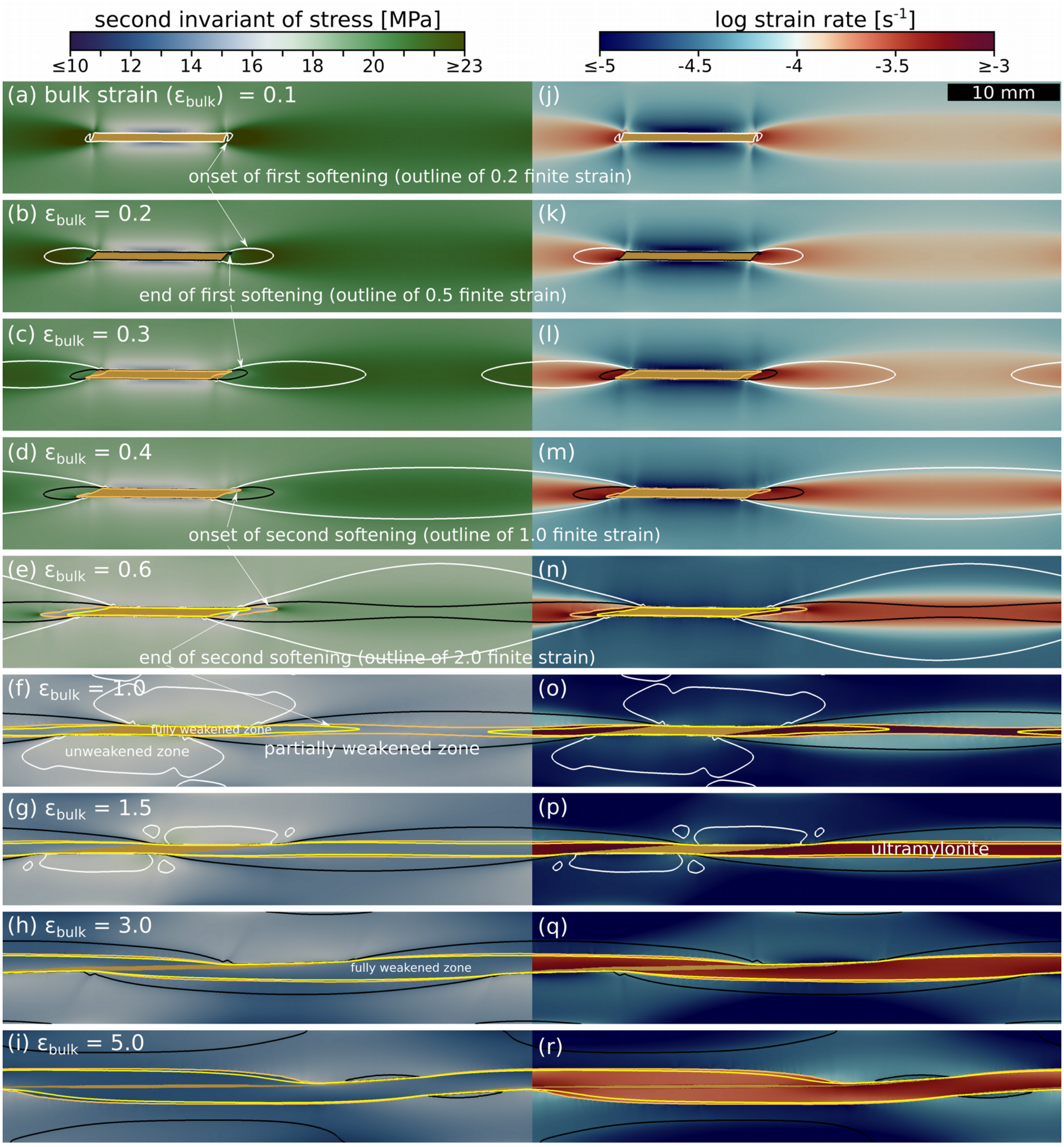

Figure 8: Local stress (a-i) and strain rate (j-r) evolution within the matrix of the ultramylonite model. Outlines indicate finite strain thresholds ε_1 = 0.2 for onset of softening (white), ε_2 = 0.5 end of first softening stage (black), ε_3 = 1.0 for beginning of second stage (orange) and, ε_4 = 2.0 for end of second (yellow) softening stage. The onset of the second softening stage triggers evolution of further localized high strain layer (e,f,n,o) representing ultramylonite formation within a mylonite.

4. Discussion

The experimentally observed formation of a localized shear zone and the rheological weakening of the Carrara marble is successfully reproduced in our numerical models with strain-dependent softening, both in terms of bulk evolution and final strain pattern. The model reaches steady state at a bulk strain of ~2 in good agreement with observations from experiments (Rybacki et al., 2014). Once steady-state is reached, grain-size reduction through dynamic recrystallization and grain growth are anticipated to compensate (De Bresser et al., 2001), resulting in steady-state material strength. Our model results provide insight into the development of local stress, strain partitioning between matrix, inclusion and shear zone and ensuing viscosities. This provides detailed insight in the evolution of a localized shear zone that allows a direct comparison with the bulk mechanical data and microstructural observations collected from the deformation experiments. Note, for example, that the model successfully predicts the local stress concentration and strain rate amplification ahead of the inclusion in excellent agreement with the experimental results. This provides confidence to the results of the parameter study performed here, as to the magnitude of softening. This holds in particular to the results of models predicting progressive multistage softening combined with a change in deformation mechanisms, as suggested from a plethora of field studies.

The advantage of employing a simple softening law is to keep numerical complexity low in order to save computational time (e.g. Huismans & Beaumont, 2003; Brune et al., 2014). Note that numerical models of brittle deformation often involve a strong mesh-dependency (De Borst & Mühlhaus, 1992) such that the softening parameters have to be adopted to the chosen resolution. However, in modeling viscous deformation, the size of the process zone as well as the bulk shear stress evolution and employed softening parameters (ε_1, ε_2, A) are almost independent of the model resolution.

The nucleation of a localized shear zone at the inclusion tips involves formation of a process zone. This process zone is defined by a strong local stress concentration and resulting volume of enhanced microstructural modification (Rybacki et al., 2014). In our models this zone is represented by a 2D area showing local stress concentrations that result from the viscosity contrast between limestone and marble present at the assumed temperature conditions. The enhanced stress levels locally reduce the effective viscosity of the Carrara marble (power-law rheology) resulting in locally increased strain rates. In turn, this triggers rheological weakening causing shear strain to progressively localize in a shear zone embedded in the Carrara matrix. A localized, elliptical process zone is established, corresponding to the experiments, that display a zone of gradually reduced grain-sizes around the inclusion tips.

Previously, in an attempt to model weakening and localization, different types of softening laws have been used aiming at parameterizing the weakening behavior of natural materials. For example, Gardner et al. (2017) studied strain localization using different load bearing framework geometries. They found that interconnected weak layers are hard to form without a dynamic weakening process, which was also observed in an experimental study by Holyoke III & Tullis (2006). This agrees with our results showing that pronounced shear zone formation in the matrix only occurs for materials with an implemented weakening formalism simulating progressive material softening. This implies the necessity of using softening laws to properly model strain localization and thus shear zone formation. Gardner et al. (2017) used a different implementation to simulate weakening. They introduced stress dependent softening combined with time dependent hardening focusing on the transition from non-linear to linear flow. At larger scale, Mazzotti & Gueydan (2017) pointed out the fundamental role of inherited tectonic structures for strain and seismicity concentrations in an intraplate setting. Similar to our study, their model also includes irreversible softening (no counteracting hardening mechanism). However, in their model softening is achieved by changing the material yield stress instead of the pre-exponential factor in a constitutive law, as in this study.

Multiple effects may play an important role affecting localization and shear zone formation in natural rocks and could be implemented in numerical models, such as shear heating (Thielmann & Kaus, 2012; Duretz et al., 2015), melting (Dannberg & Heister, 2016; Schmeling et al., 2018) or a switch to grain-size sensitive diffusion creep, like modeled in our study (e.g. Handy, 1989). Studying non-homogeneous composite materials, material intrinsic softening as modeled in this study needs to be complemented with structural or geometric softening (e.g. layering or fault reactivation) of the entire composite (Duretz et al., 2016).

Benchmarking of our numerical models to laboratory experiments forms the basis for a parameter study that allows exploring effects such as viscosity contrast between shear zone materials and matrix. This allows to go beyond what can be observed in the lab. In that sense, we elucidate the process of ultramylonite formation (Figure 8), which is achieved by introducing a second softening stage that mimics the transition to diffusion creep and grain boundary sliding (e.g. Cross & Skemer, 2017). Implementing a single inclusion model captures the nested structure and shape of the resulting high-strain band, which is in good agreement with common observations of ultramylonite bands in nature (Heitzmann, 1987; Kilian et al., 2011).

5. Conclusions

Strength reduction of rocks associated with strain localization in shear zones is an important process in lithosphere dynamics occurring over a broad range of spatial scales. The process is tied to weakening mechanisms acting on the grain scale. For simplicity, we use a piece-wise linear softening law and show that it is capable of simulating rheological weakening. This allows establishing a minimum constraint on viscous strain softening. Our model provides a virtual way of analyzing the viscous process zone evolution that can be divided into four phases (P1) *pre-weakening*, (P2) *onset and acceleration of weakening*, (P3) *deceleration of weakening* and (P4) *steady-state*. Spatial stress distributions show that matrix strain localization is initiated by a local stress peak at the inclusion tips. From there and with increasing strain, the process zone expands into the matrix. Shear zone width and localization rate are controlled by the amount of rheological weakening. Our numerical models show that rheological weakening is necessary to establish a pronounced shear zone in a strong matrix surrounding a weak inclusion. This stresses the importance for geodynamic models to contain softening laws that appropriately account for rheological weakening.

Acknowledgments

This study was conducted within the Helmholtz Young Investigators Group CRYSTALS (VH-NG-1132). Laboratory experiments were performed in Geomechanics and Rheology section of the German Research Centre for Geosciences and we thank Stefan Gehrmann for help with sample preparation. Simulations were performed on the cluster facilities of the German Research Centre for Geosciences. Figures were created using Paraview and Matlab and color maps were taken from Crameri (2018).

References

Barnhoorn, A., Bystricky, M., Burlini, L., & Kunze, K. (2004). The role of recrystallisation on the deformation behaviour of calcite rocks: Large strain torsion experiments on Carrara marble. *Journal of Structural Geology*, *26*(5), 885–903. https://doi.org/10.1016/j.jsg.2003.11.024

Bonet, J., & Wood, R. D. (1997). *Nonlinear Continuum Mechanics for Finite Element Analysis*. Cambridge University Press. https://doi.org/10.1017/CBO9780511755446

Bruhn, D. F., & Casey, M. (1997). Texture development in experimentally deformed two-phase aggregates of calcite and anhydrite. *Journal of Structural Geology*, *19*(7), 909–925. https://doi.org/10.1016/S0191-8141(97)00023-0

Bruhn, D. F., Olgaard, D. L., & Dell'Angelo, L. N. (1999). Evidence for enhanced deformation in two-phase rocks: Experiments on the rheology of calcite-anhydrite aggregates. *Journal of Geophysical Research*, *104*(B1), 707. https://doi.org/10.1029/98JB02847

Brune, S. (2014). Evolution of stress and fault patterns in oblique rift systems: 3-D numerical lithospheric-scale experiments from rift to breakup. *Geochemistry, Geophysics, Geosystems*, *15*(8), 3392–3415. https://doi.org/10.1002/2014GC005446

Brune, S., & Autin, J. (2013). The rift to break-up evolution of the Gulf of Aden: Insights from 3D numerical lithospheric-scale modelling. *Tectonophysics*, *607*, 65–79. https://doi.org/10.1016/j.tecto.2013.06.029

Brune, S., Heine, C., Clift, P. D., & Pérez-Gussinyé, M. (2017). Rifted margin architecture and crustal rheology: Reviewing Iberia-Newfoundland, Central South Atlantic, and South China Sea. *Marine and Petroleum Geology*, *79*, 257–281. https://doi.org/10.1016/j.marpetgeo.2016.10.018

Brune, S., Heine, C., Pérez-Gussinyé, M., & Sobolev, S. V. (2014). Rift migration explains continental margin asymmetry and crustal hyper-extension. *Nature Communications*, *5*, 1–9. https://doi.org/10.1038/ncomms5014

Brune, S., Popov, A. A., & Sobolev, S. V. (2012). Modeling suggests that oblique extension facilitates rifting and continental break-up. *Journal of Geophysical Research: Solid Earth*, *117*(8), 1–16. https://doi.org/10.1029/2011JB008860

Brune, S., Popov, A. A., & Sobolev, S. V. (2013). Quantifying the thermo-mechanical impact of plume arrival on continental break-up. *Tectonophysics*, *604*(3), 51–59. https://doi.org/10.1016/j.tecto.2013.02.009

Brune, S., Williams, S. E., Butterworth, N. P., & Müller, R. D. (2016). Abrupt plate accelerations shape rifted continental margins. *Nature*, 1–4. https://doi.org/10.1038/nature18319

Bürgmann, R., & Dresen, G. (2008). Rheology of the Lower Crust and Upper Mantle: Evidence from Rock Mechanics, Geodesy, and Field Observations. *Annu. Rev. Earth Planet. Sci.*, *36*(1), 531–567. https://doi.org/10.1146/annurev.earth.36.031207.124326

Burlini, L., & Bruhn, D. (2005). High-strain zones: laboratory perspectives on strain softening during ductile deformation. *Geological Society, London, Special Publications*, *245*(1), 1–24. https://doi.org/10.1002/2017JB014333

Bystricky, M., Heidelbach, F., & Mackwell, S. (2006). Large-strain deformation and strain partitioning in polyphase rocks: Dislocation creep of olivine-magnesiowüstite aggregates. *Tectonophysics*, *427*(1–4), 115–132. https://doi.org/10.1016/j.tecto.2006.05.025

Bystricky, M., Kunze, K., Burlini, L., & Burg, J.-P. (2000). High Shear Strain of Olivine Aggregates: Rheological and Seismic Consequences. *Science*, *290*(5496), 1564–1567. https://doi.org/10.1126/science.290.5496.1564

Clift, P. D., Brune, S., & Quinteros, J. (2015). Climate changes control offshore crustal structure at South China Sea continental margin. *Earth and Planetary Science Letters*, *420*, 66–72. https://doi.org/10.1016/j.epsl.2015.03.032

Cook, A. C., Vel, S. S., Gerbi, C., & Johnson, S. E. (2014). Computational analysis of nonlinear creep of polyphase aggregates: Influence of phase morphology. *Journal of Geophysical Research B: Solid Earth*, *119*(9), 6877–6906. https://doi.org/10.1002/2014JB011197

Corti, G., van Wijk, J., Cloetingh, S., & Morley, C. K. (2007). Tectonic inheritance and continental rift architecture: Numerical and analogue models of the East African Rift system. *Tectonics*, *26*(6), 1–13. https://doi.org/10.1029/2006TC002086

Coyan, M. M., Arrowsmith, J. R., Umhoefer, P., Coyan, J., Kent, G., Driscoll, N., & Gutíerrez, G. M. (2013). Geometry and quaternary slip behavior of the San Juan de los Planes and Saltito fault zones, Baja California Sur, Mexico: Characterization of rift-margin normal faults. *Geosphere*, *9*(3), 426–443. https://doi.org/10.1130/GES00806.1

Crameri, F. (2018). Geodynamic diagnostics, scientific visualisation and StagLab 3.0. *Geoscientific Model Development Discussions*, (February), 1–41. https://doi.org/10.5194/gmd-2017-328

Cross, A. J., Ellis, S., & Prior, D. J. (2015). A phenomenological numerical approach for investigating grain size evolution in ductiley deforming rocks. *Journal of Structural Geology*, *76*, 22–34. https://doi.org/10.1016/j.jsg.2015.04.001

Cross, A. J., & Skemer, P. (2017). Ultramylonite generation via phase mixing in high-strain experiments. *Journal of Geophysical Research: Solid Earth*, *122*(3), 1744–1759. https://doi.org/10.1002/2016JB013801

Cyprych, D., Brune, S., Piazolo, S., & Quinteros, J. (2016). Strain localization in polycrystalline material with second phase particles: Numerical modeling with application to ice mixtures. *Geochemistry, Geophysics, Geosystems*, *17*(9), 3608–3628. https://doi.org/10.1002/2016GC006471

Dannberg, J., & Heister, T. (2016). Compressible magma/mantle dynamics: 3-D, adaptive simulations in ASPECT. *Geophysical Journal International*, *207*(3), 1343–1366. https://doi.org/10.1093/gji/ggw329

De Borst, R., & Mühlhaus, H. B. (1992). Gradient‐dependent plasticity: Formulation and algorithmic aspects. *International Journal for Numerical Methods in Engineering*, *35*(3), 521–539. https://doi.org/10.1002/nme.1620350307

De Bresser, J. H. P., Ter Heege, J. H., & Spiers, C. J. (2001). Grain size reduction by dynamic recrystallization: Can it result in major rheological weakening? *International Journal of Earth Sciences*, *90*(1), 28–45. https://doi.org/10.1007/s005310000149

Dimanov, A., & Dresen, G. (2005). Rheology of synthetic anorthite-diopside aggregates: Implications for ductile shear zones. *Journal of Geophysical Research: Solid Earth*, *110*(7), 1–24. https://doi.org/10.1029/2004JB003431

Duesterhoeft, E., Quinteros, J., Oberhänsli, R., Bousquet, R., & de Capitani, C. (2014). Relative impact of mantle densification and eclogitization of slabs on subduction dynamics: A numerical thermodynamic/thermokinematic investigation of metamorphic density evolution. *Tectonophysics*, *637*, 20–29. https://doi.org/10.1016/j.tecto.2014.09.009

Duretz, T., Petri, B., Mohn, G., Schmalholz, S. M., Schenker, F. L., & Müntener, O. (2016). The importance of structural softening for the evolution and architecture of passive margins. *Scientific Reports*, *6*(May), 1–7. https://doi.org/10.1038/srep38704

Duretz, T., Schmalholz, S. M., & Podladchikov, Y. Y. (2015). Shear heating-induced strain localization across the scales. *Philosophical Magazine*, *95*(28–30), 3192–3207. https://doi.org/10.1080/14786435.2015.1054327

Ellis, S., Wissing, S., & Pfiffner, A. (2001). Strain localization as a key to reconciling experimentally derived flow-law data with dynamic models of continental collision. *International Journal of Earth Sciences*, *90*(1), 168–180. https://doi.org/10.1007/s005310000151

Fossen, H., & Cavalcante, G. C. G. (2017). Shear zones – A review. *Earth-Science Reviews*, *171*(January), 434–455. https://doi.org/10.1016/j.earscirev.2017.05.002

Gardner, R., Piazolo, S., Evans, L., & Daczko, N. (2017). Patterns of strain localization in heterogeneous, polycrystalline rocks – a numerical perspective. *Earth and Planetary Science Letters*, *463*, 253–265. https://doi.org/10.1016/j.epsl.2017.01.039

Gerbi, C., Johnson, S. E., Cook, A., & Vel, S. S. (2015). Effect of phase morphology on bulk strength for power-law materials. *Geophysical Journal International*, *200*(1), 374–389. https://doi.org/10.1093/gji/ggu388

Gueydan, F., Précigout, J., & Montési, L. G. J. (2014). Strain weakening enables continental plate tectonics. *Tectonophysics*, *631*(C), 189–196. https://doi.org/10.1016/j.tecto.2014.02.005

Handy, M. R. (1989). Deformation regimes and the rheological evolution of fault zones in the lithosphere: the effects of pressure, temperature, grainsize and time. *Tectonophysics*, *163*(1–2), 119–152. https://doi.org/10.1016/0040-1951(89)90122-4

Handy, M. R., Mulch, A., Rosenau, M., & Rosenberg, C. L. (2001). The role of fault zones and melts as agents of weakening, hardening and differentiation of the continental crust: a synthesis. *Geological Society, London*, *Special Publications*, *186*(1), 305–332. https://doi.org/10.1144/GSL.SP.2001.186.01.18

Hansen, L. N., Zimmerman, M. E., Dillman, A. M., & Kohlstedt, D. L. (2012). Strain localization in olivine aggregates at high temperature: A laboratory comparison of constant-strain-rate and constant-stress boundary conditions. *Earth and Planetary Science Letters*, *333–334*, 134–145. https://doi.org/10.1016/j.epsl.2012.04.016

Heine, C., & Brune, S. (2014). Oblique rifting of the equatorial atlantic: Why there is no saharan atlantic ocean. *Geology*, *42*(3), 211–214. https://doi.org/10.1130/G35082.1

Heitzmann, P. (1987). Calcite mylonites in the central root zone. *Tectonophysics*, *135*, 207–215. https://doi.org/10.1016/0040-1951(87)90162-4

Herwegh, M., Poulet, T., Karrech, A., & Regenauer-Lieb, K. (2014). From transient to steady state deformation and grain size: A thermodynamic approach using elasto-visco-plastic numerical modeling. *Journal of Geophysical Research: Solid Earth*, *119*(2), 900–918. https://doi.org/10.1002/2013JB010701

Hippertt, J. F., & Hongn, F. D. (1998). Deformation mechanisms in the mylonite/ultramylonite transition. *Journal of Structural Geology*, *20*(11), 1435–1448. https://doi.org/10.1016/S0191-8141(98)00047-9

Holyoke III, C. W., & Tullis, J. (2006). Mechanisms of weak phase interconnection and the effects of phase strength contrast on fabric development. *Journal of Structural Geology*, *28*(4), 621–640. https://doi.org/10.1016/j.jsg.2006.01.008

Huismans, R. S., & Beaumont, C. (2003). Symmetric and asymmetric lithospheric extension: Relative effects of frictional-plastic and viscous strain softening. *Journal of Geophysical Research: Solid Earth*, *108*(B10), 1–22. https://doi.org/10.1029/2002JB002026

Jammes, S., Lavier, L. L., & Reber, J. E. (2015). Localization and delocalization of deformation in a bimineralic material. *Journal of Geophysical Research: Solid Earth*, *120*(5), 3649–3663. https://doi.org/10.1002/2015JB011890

Jessell, M. W., Siebert, E., Bons, P. D., Evans, L., & Piazolo, S. (2005). A new type of numerical experiment on the spatial and temporal patterns of localization of deformation in a material with a coupling of grain size and rheology. *Earth and Planetary Science Letters*, *239*(3–4), 309–326. https://doi.org/10.1016/j.epsl.2005.03.030

Ji, S., Jiang, Z., Rybacki, E., Wirth, R., Prior, D., & Xia, B. (2004). Strain softening and microstructural evolution of anorthite aggregates and quartz-anorthite layered composites deformed in torsion. *Earth and Planetary Science Letters*, *222*(2), 377–390. https://doi.org/10.1016/j.epsl.2004.03.021

Kenkmann, T., & Dresen, G. (1998). Stress gradients around porphyroclasts: palaeopiezometric estimates and numerical modelling. *Journal of Structural Geology*, *20*(213), 163–173. https://doi.org/10.1016/S0191-8141(97)00074-6

Kenkmann, T., & Dresen, G. (2002). Dislocation microstructure and phase distribution in a lower crustal shear zone - An example from the Ivrea-Zone, Italy. *International Journal of Earth Sciences*, *91*(3), 445–458. https://doi.org/10.1007/s00531-001-0236-9

Kilian, R., Heilbronner, R., & Stünitz, H. (2011). Quartz grain size reduction in a granitoid rock and the transition from dislocation to diffusion creep. *Journal of Structural Geology*, *33*(8), 1265–1284. https://doi.org/10.1016/j.jsg.2011.05.004

Koopmann, H., Brune, S., Franke, D., & Breuer, S. (2014). Linking rift propagation barriers to excess magmatism at volcanic rifted margins. *Geology*, *42*(12), 1071–1074. https://doi.org/10.1130/G36085.1

Linckens, J., Herwegh, M., Mntener, O., & Mercolli, I. (2011). Evolution of a polymineralic mantle shear zone and the role of second phases in the localization of deformation. *Journal of Geophysical Research: Solid Earth*, *116*(B6). https://doi.org/10.1029/2010JB008119

Mancktelow, N. S. (2002). Finite-element modelling of shear zone development in viscoelastic materials and its implications for localisation of partial melting. *Journal of Structural Geology*, *24*(6–7), 1045–1053. https://doi.org/10.1016/S0191-8141(01)00090-6

Mancktelow, N. S., & Pennacchioni, G. (2005). The control of precursor brittle fracture and fluid-rock interaction on the development of single and paired ductile shear zones. *Journal of Structural Geology*, *27*(4), 645–661. https://doi.org/10.1016/j.jsg.2004.12.001

Mazzotti, S., & Gueydan, F. (2017). Control of tectonic inheritance on continental intraplate strain rate and seismicity. *Elsevier*. https://doi.org/10.1016/j.tecto.2017.12.014

Misra, S., & Mandal, N. (2007). Localization of plastic zones in rocks around rigid inclusions: Insights from experimental and theoretical models. *Journal of Geophysical Research: Solid Earth*, *112*(9), 1–15. https://doi.org/10.1029/2006JB004328

Nardini, L., Rybacki, E., Morales, L. G., & Dresen, G. (2018). Effect of different loading conditions on the nucleation and development of shear zones around material heterogeneities. In *TSG and MSG Joint Conference Abstracts*.

Okada, Y. (1985). Surface deformation due to shear and tensile faults in a half-space. *Bulletin of the Seismological Society of America*, *75*(4), 1135–1154. Retrieved from https://pubs.geoscienceworld.org/ssa/bssa/article/75/4/1135/118782/surface-deformation-due-to-shear-and-tensile

Palin, R. M., Searle, M. P., St-Onge, M. R., Waters, D. J., Roberts, N. M. W., Horstwood, M. S. A., … Weller, O. M. (2014). Two-stage cooling history of pelitic and semi-pelitic mylonite (sensu lato) from the Dongjiu-Milin shear zone, northwest flank of the eastern Himalayan syntaxis. *Gondwana Research*, *28*(2), 509–530. https://doi.org/10.1016/j.gr.2014.07.009

Park, M., & Jung, H. (2017). Microstructural evolution of the Yugu peridotites in the Gyeonggi Massif, Korea: Implications for olivine fabric transition in mantle shear zones. *Tectonophysics*, *709*, 55–68. https://doi.org/10.1016/j.tecto.2017.04.017

Paterson, M. S. (1970). A high-pressure, high-temperature apparatus for rock deformation. *International Journal of Rock Mechanics and Mining Sciences And*, *7*(5), 517–526. https://doi.org/10.1016/0148-9062(70)90004-5

Paterson, M. S., & Olgaard, D. L. (2000). Rock deformation tests to large shear strains in torsion. *Journal of Structural Geology*, *22*(9), 1341–1358. https://doi.org/10.1016/S0191-8141(00)00042-0

Pieri, M., Burlini, L., Kunze, K., Stretton, I., & Olgaard, D. L. (2001a). Rheological and microstructural evolution of Carrara marble with high shear strain: results from high temperature torsion experiments. *Journal of Structural Geology*, *23*(9), 1393–1413. https://doi.org/10.1016/S0191-8141(01)00006-2

Pieri, M., Kunze, K., Burlini, L., Stretton, I., Olgaard, D. L., Burg, J.-P., & Wenk, H.-R. (2001b). Texture development of calcite by deformation and dynamic recrystallization at 1000 K during torsion experiments of marble to large strains. *Tectonophysics*, *330*(1–2), 119–140. https://doi.org/10.1016/S0040-1951(00)00225-0

Popov, A. A., & Sobolev, S. V. (2008). SLIM3D: A tool for three-dimensional thermomechanical modeling of lithospheric deformation with elasto-visco-plastic rheology. *Physics of the Earth and Planetary Interiors*, *171*, 55–75. https://doi.org/10.1016/j.pepi.2008.03.007

Popov, A. A., Sobolev, S. V., & Zoback, M. D. (2012). Modeling evolution of the San Andreas Fault system in northern and central California. *Geochemistry, Geophysics, Geosystems*, *13*(8), 1–21. https://doi.org/10.1029/2012GC004086

Quinteros, J., & Sobolev, S. V. (2013). Why has the Nazca plate slowed since the Neogene? *Geology*, *41*(1), 31–34. https://doi.org/10.1130/G33497.1

Quinteros, J., Sobolev, S. V., & Popov, A. A. (2010). Viscosity in transition zone and lower mantle: Implications for slab penetration. *Geophysical Research Letters*, *37*(9). https://doi.org/10.1029/2010GL043140

Rutter, E. H. (1999). On the relationship between the formation of shear zones and the form of the flow law for rocks undergoing dynamic recrystallization. *Tectonophysics*, *303*(1–4), 147–158. https://doi.org/10.1016/S0040-1951(98)00261-3

Rybacki, E., Morales, L. F. G., Naumann, M., & Dresen, G. (2014). Strain localization during high temperature creep of marble: The effect of inclusions. *Tectonophysics*, *634*(September 2014), 182–197. https://doi.org/10.1016/j.tecto.2014.07.032

Rybacki, E., Paterson, M. S., Wirth, R., & Dresen, G. (2003). Rheology of calcite–quartz aggregates deformed to large strain in torsion. *Journal of Geophysical Research-Solid Earth*, *108*(B2), 2089. https://doi.org/10.1029/2002JB001833

Schmeling, H., Marquart, G., & Grebe, M. (2018). A porous flow approach to model thermal non-equilibrium applicable to melt migration. *Geophysical Journal International*, *212*(1), 119–138. https://doi.org/10.1093/gji/ggx406

Schmid, S. M., Paterson, M. S., & Boland, J. N. (1980). High temperature flow and dynamic recrystallization in Carrara marble. *Tectonophysics*, *65*, 245–280. https://doi.org/10.1016/0040-1951(80)90077-3

Simo, J. C., & Hughes, T. J. (2006). *Computational inelasticity*. Springer Science & Business Media.

Tasaka, M., Zimmerman, M. E., Kohlstedt, D. L., Stünitz, H., & Heilbronner, R. (2017). Rheological Weakening of Olivine + Orthopyroxene Aggregates Due To Phase Mixing: Part 2. Microstructural Development. *Journal of Geophysical Research: Solid Earth*, *122*(10), 7597–7612. https://doi.org/10.1002/2017JB014311

Ter Heege, J. H., De Bresser, J. H. P., & Spiers, C. J. (2001). The influence of dynamic recrystallization on the grain size distribution and rheological behaviour of Carrara marble deformed in axial compression. *Geological Society, London, Special Publications*, *200*(1), 331–353. https://doi.org/10.1144/GSL.SP.2001.200.01.19

Thielmann, M., & Kaus, B. J. P. (2012). Shear heating induced lithospheric-scale localization: Does it result in subduction? *Earth and Planetary Science Letters*, *359–360*, 1–13. https://doi.org/10.1016/j.epsl.2012.10.002

Treagus, S. H., & Lan, L. (2004). Deformation of square objects and boudins. *Journal of Structural Geology*, *26*(8), 1361–1376. https://doi.org/10.1016/j.jsg.2003.12.002

Valoroso, L., Chiaraluce, L., Piccinini, D., Di Stefano, R., Schaff, D., & Waldhauser, F. (2013). Radiography of a normal fault system by 64,000 high-precision earthquake locations: The 2009 L'Aquila (central Italy) case study. *Journal of Geophysical Research: Solid Earth*, *118*(3), 1156–1176. https://doi.org/10.1002/jgrb.50130

Webber, S., Ellis, S., & Fagereng, Å. (2018). "Virtual shear box" experiments of stress and slip cycling within a subduction interface mélange. *Earth and Planetary Science Letters*, *488*, 27–35. https://doi.org/10.1016/j.epsl.2018.01.035

White, S. (1976). A Discussion on natural strain and geological structure - The effects of strain on the microstructures, fabrics, and deformation mechanisms in quartzites. *Philosophical Transactions for the Royal Society of London A.*, *283*(1312), 69–86. https://doi.org/10.1098/rsta.1976.0070

Zang, A., Wagner, F. C., Stanchits, S., Janssen, C., & Dresen, G. (2000). Fracture process zone in granite. *Journal of Geophysical Research: Solid Earth*, *105*(B10), 23651–23661. https://doi.org/10.1029/2000JB900239

JGR-Solid Earth

Supporting Information for

Strain Localization and Weakening Processes in Viscously Deforming Rocks: Numerical Modeling Based on Laboratory Torsion Experiments

M. J. E. A. Döhmann[1,2*], S. Brune[1,2], L. Nardini[1], E. Rybacki[1], G. Dresen[1,2]

[1]GFZ German Research Centre for Geosciences, Telegrafenberg, 14473 Potsdam, Germany

[2]Institute of Earth and Environmental Sciences, University of Potsdam, Germany

* Corresponding author: Maximilian Döhmann (doehmann@gfz-potsdam.de)

Contents of this file

Figures S1 to S2

Movies S3 to S4

Additional Supporting Information (Files uploaded separately)

Captions for Movies S3 to S4

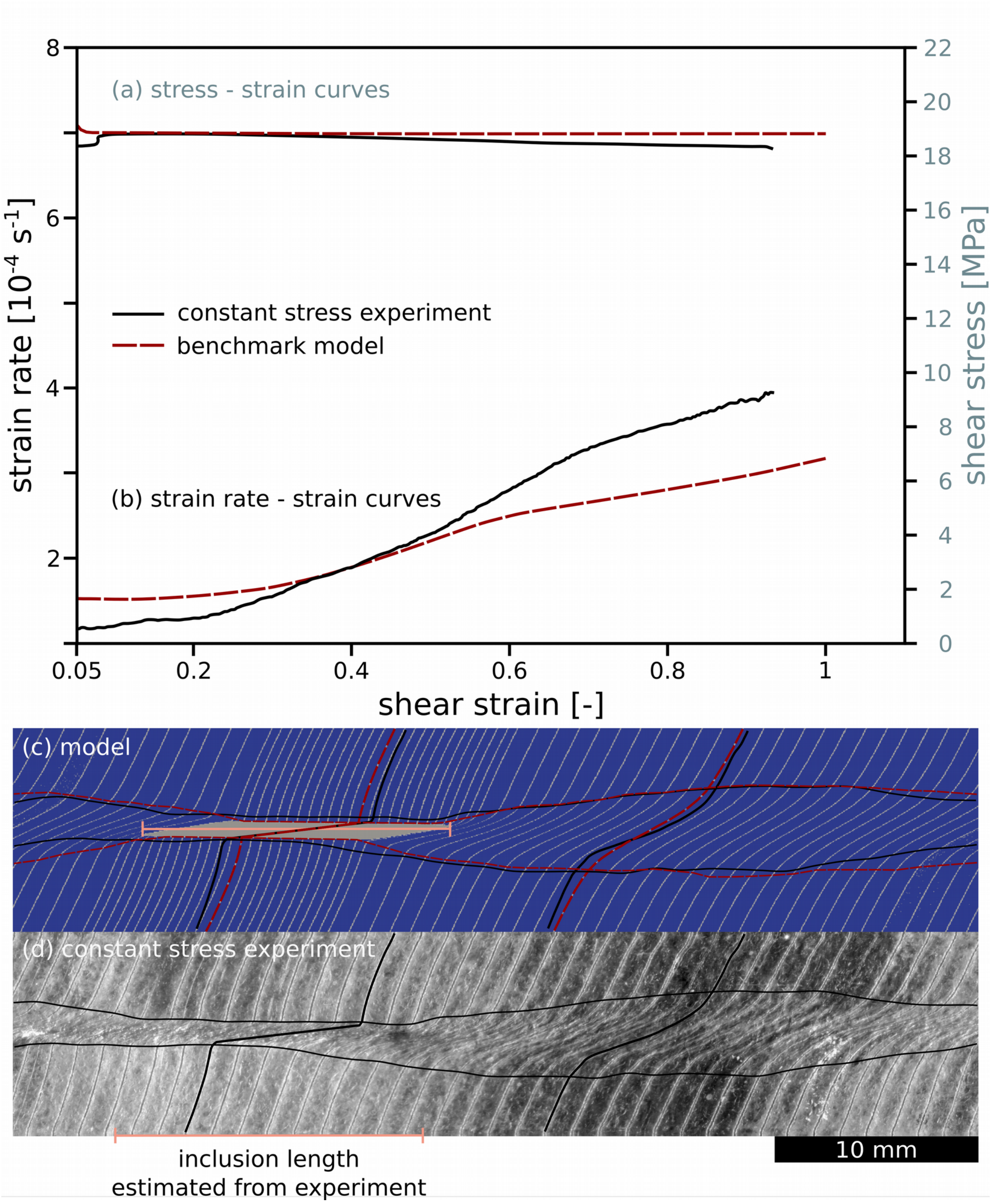

Figure S1. Comparison of constant stress model to experiment. (a) Stress strain curves of model (red) and experiment (black). (b) Strain rate plot over strain. (c) Model with passive strain markers and shear zone outlines of model (red) and experiment (black). (c) Copper jacket from experiment with passive strain markers, estimated inclusion length and shear zone outline. Results in (c) and (d) are shown at a bulk shear strain of 0.93.

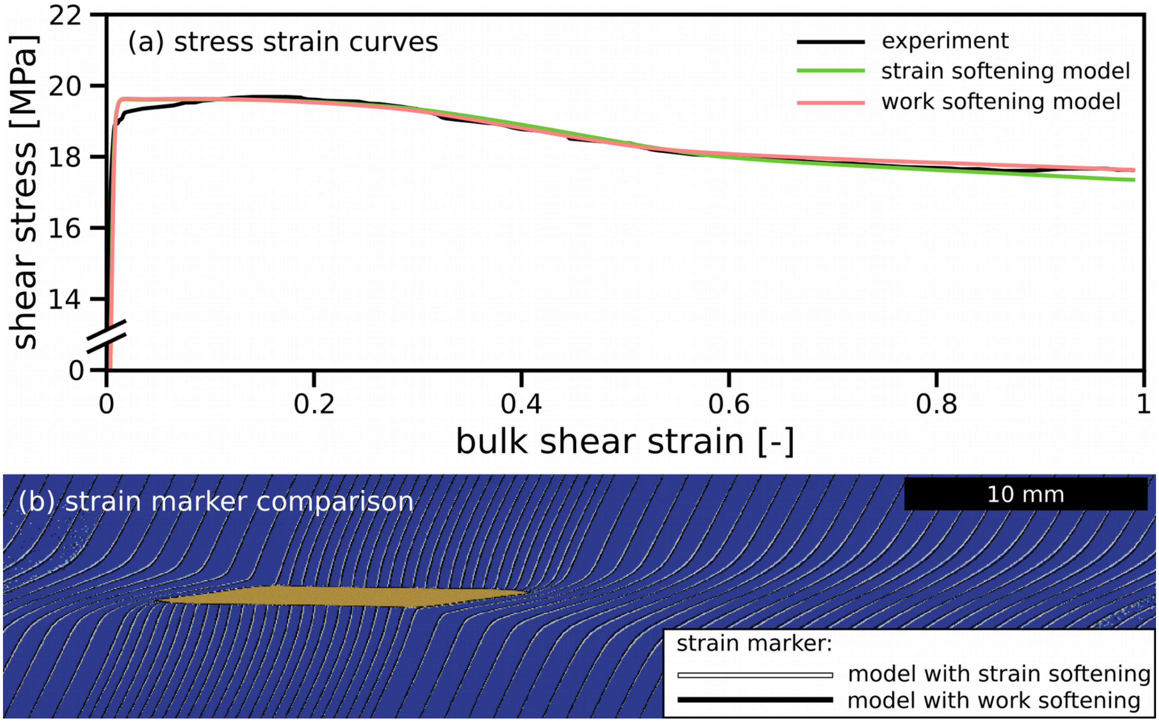

Figure S2. Comparison of strain and deformation work based weakening implementations with constant strain rate boundary conditions. (a) Stress strain curves of strain weakening model (green), work weakening (purple) and experiment (black). (b) Strain marker comparison between strain dependent (white) and work dependent (black) implementation of softening, showing almost identical results.

Movie S3. Benchmark model evolution.

Movie S4. Ultramylonite model evolution.